

pubs.acs.org/ac Article

Advancing Protein Analysis: A Low-Pressure Drift Tube Orbitrap Mass Spectrometer for Ultraviolet Photodissociation-Based Structural Characterization

Jamie P. Butalewicz, James D. Sanders, Kyle J. Juetten, Nathan W. Buzitis, Brian H. Clowers, and Jennifer S. Brodbelt*



Cite This: Anal. Chem. 2024, 96, 15674-15681



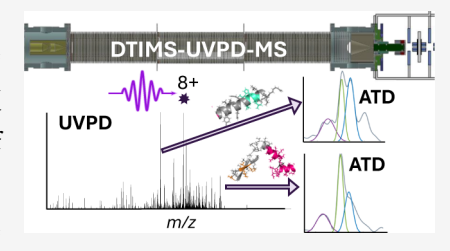
ACCESS I

III Metrics & More

Article Recommendations

Supporting Information

ABSTRACT: Owing to its ability to generate extensive fragmentation of proteins, ultraviolet photodissociation (UVPD) mass spectrometry (MS) has emerged as a versatile ion activation technique for the structural characterization of native proteins and protein complexes. Interpreting these fragmentation patterns provides insight into the secondary and tertiary structures of protein ions. However, the inherent complexity and diversity of proteins often pose challenges in resolving their numerous conformations. To address this limitation, we combined UVPD-MS with drift tube ion mobility, offering potential to acquire conformationally selective MS/MS information. A low-pressure drift tube (LPDT) Orbitrap mass spectrometer equipped with 193 nm UVPD capabilities enables



the analysis of protein conformers through the analysis of arrival time distributions (ATDs) of individual fragment ions. ATDs of fragment ions are compared for different backbone cleavage sites of the protein or different precursor charge states to give information about regions of potential folding or elongation. This integrated platform offers promise for advancing our understanding of protein structures in the gas phase.

■ INTRODUCTION

The coupling of ion mobility spectrometry (IMS) with mass spectrometry (MS) has found broad applications in the characterization of a wide variety of biological molecules, ranging from small molecules, 1-3 lipids, 4-6 and peptides 7-10 to intact proteins 11-15 and multimeric protein complexes. 16-18 The majority of IMS-MS systems utilize time-of-flight (TOF) mass analyzers. While the kHz scan rates of TOF analyzers adequately sample IM separations occurring at tens of Hz, such instrument combinations do not necessarily provide the highest m/z resolution or the most versatile MS/MS capabilities, thus hindering their utility for the analysis of complex biomolecules. Orbitrap MS platforms offer higher resolutions and highperformance MS/MS capabilities such as hybrid activation methods like EThcD²⁰ and AI-ETD,²¹ or ultraviolet photo-dissociation (UVPD).^{22–26} However, coupling drift tube IMS to higher resolution trapping-based mass analyzers, such as Fourier transform ion cyclotron resonance and Orbitrap mass analyzers, requires the consideration of the fact that these detectors operate too slowly to sample ions in real time as they exit the drift tube. 15,27-30

This duty cycle mismatch necessitates the use of electrostatic ion gates to control the flow of ions into and out of the drift region of the IMS, so that ions with a particular drift time can be selectively transmitted to the mass spectrometer for analysis. When these gates are operated in Fourier or Hadamard transform multiplexing modes, dual-gate IM—MS instruments can generate high-quality arrival time distributions (ATDs),

while maintaining ion utilization of up to 25% without the need for front-end ion trapping. ^{15,31,32} Both atmospheric-pressure and reduced-pressure drift tubes have been coupled with Orbitrap mass spectrometers and successfully deployed for a wide variety of analytical targets ranging from small molecules to intact protein complexes. ^{28,33–35} In one notable design, FT multiplexing was used to integrate a custom-built drift tube with an extended mass range Orbitrap mass spectrometer, and its utility was demonstrated for native top-down MS. ^{15,34} This system used a novel rear entry source that preserved the high-resolution mass analysis of the Orbitrap analyzer and allowed the determination of collision cross sections and MS/MS analysis of intact protein complexes.

Combining IMS with new ion activation methods offers another intriguing strategy to expand the capabilities and applications of IM separations. UVPD generates rich and structurally informative fragmentation patterns for a wide variety of biomolecules, including both smaller molecules like peptides, lipids, carbohydrates, and nucleic acids, and larger molecules like proteins 22,23,36-38 and protein complexes. ³⁹⁻⁴² In

Received: June 18, 2024
Revised: August 15, 2024
Accepted: September 4, 2024
Published: September 16, 2024





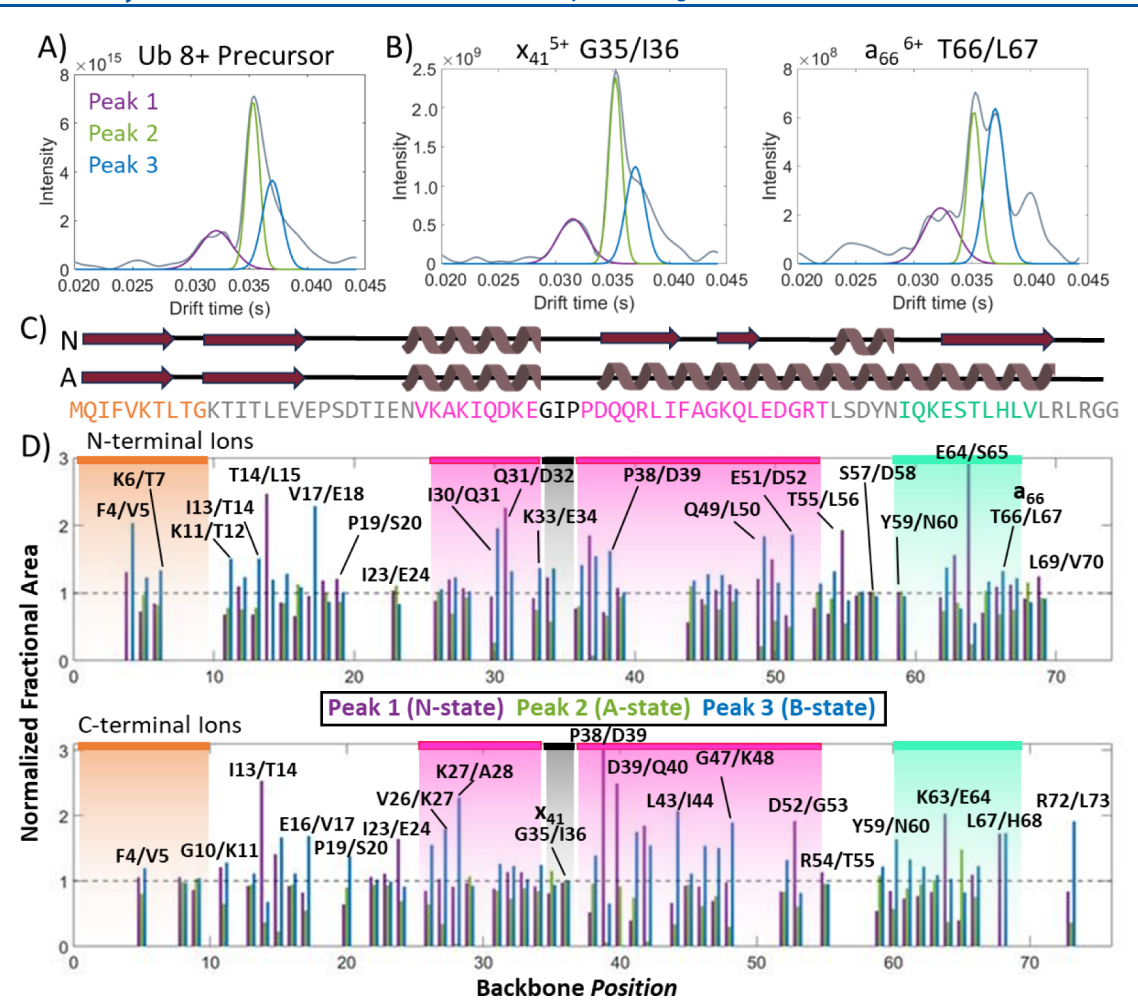


Figure 1. A) Precursor ATD for the 8+ charge state of ubiquitin fits to three Gaussian peaks (purple, green, blue). The unprocessed ATD is shown in gray. B) Examples of ATDs, generated from two fragments (x_{41}^{5+} and a_{66}^{6+}) of the 8+ charge state of ubiquitin, fit to the same three Gaussian peaks (purple, green, and blue, with the unprocessed ATD in gray), allowing the widths to vary based on the fit. C) Sequence of ubiquitin. The secondary structural motifs are also rendered above the sequence, with thick arrows and zigzags corresponding to β-strands and α-helices, respectively. D) The entire set of ATD data is converted to a histogram, where the heights of the bars represent a normalized fractional area for the given fragment ion. The normalized fractional area is generated through the summation of all three peak areas for each fragment and comparison to the peak areas generated for the precursor ion, allowing for direct comparisons between fragment ions with different relative intensities. ATD peak areas are mapped based on the backbone site that is cleaved to generate each fragment ion. Peak 1 (purple) corresponds to the N-state, Peak 2 (green) corresponds to the A-state, and Peak 3 (blue) corresponds to the B-state. Each bar is labeled with the identity of the fragment ion and the pair of residues cleaved. The sequence of ubiquitin is displayed across the top of the histogram with colors corresponding to matching regions of the protein structure, further detailed in Figure 2.

addition to providing primary sequence information and localization of post-translational modifications, UVPD fragmentation patterns offer insights into higher-order protein structures, as well as the stoichiometry and connectivity of multimeric protein complexes.³⁹⁻⁴² For this reason, methods that can generate structurally diagnostic UVPD mass spectra of mobility-separated isomeric structures offer the potential to extend the depth of information captured from structurally complex biological molecules. UVPD of mobility-selected protein conformers produces distinct fragmentation patterns that, when mapped onto the three-dimensional structures of the targeted proteins, reveal conformational differences attributed to cis/trans isomerization of proline 43,44 and differences in unfolding pathways. 45,46 However, since these prior studies were undertaken using TOF mass analyzers without multiplexing, both the mass resolving power and ion utilization were somewhat limited. Combining FT multiplexing with a UVPDenabled linear ion trap enabled mobility-dependent photo-

dissociation of tetrasaccharide ions across all drift times simultaneously. 47 More recently, the capacity to generate ATDs of individual lipid isomers from mixtures was demonstrated on an Orbitrap system, even when they could not be resolved in the mobility dimension owing to their small differences in CCS. 48

The FT multiplexing IM—UVPD studies noted above both employed atmospheric pressure drift tubes mounted in place of the standard ESI source on commercial ion trap or Orbitrap instruments. 47,48 While this configuration is convenient in its small size, ease of installation, and respectable resolving power, convenience comes at the expense of poor ion transmission between the drift tube and the mass spectrometer. Ion loss is primarily due to the difficulty in refocusing the diffuse ion cloud leaving the drift tube, such that the ions are successfully transferred into the mass spectrometer through a 0.5 mm ion transfer tube. While the ion populations that do make it into the mass spectrometer are adequate for UVPD of smaller molecules

such as polysaccharides and lipids, UVPD of large proteins and protein complexes requires much higher ion populations due to the dilution of product ion signals between hundreds of dissociation pathways. The interest in characterizing the structures of conformationally resolved protein ions by UVPD was the primary motivation for the present work, which entailed the construction of a low-pressure uniform-field drift tube with dual RF ion funnels that can provide front-end mobility separations with minimal to no loss of ion current. Here, we describe the design and construction of this instrument built with low-cost printed circuit board (PCB) electrodes and designed to interface with multiple Orbitrap platforms and its application for the structural characterization of conformationally heterogeneous protein ions by mobility-resolved UVPD.

■ EXPERIMENTAL SECTION

Materials and Reagents. All proteins were purchased from Sigma-Aldrich (St. Louis, MO). Bovine ubiquitin from erythrocytes and myoglobin from equine skeletal muscles were used without further purification and dissolved in 50/50 methanol/water with 0.1% formic acid to a final concentration of $10~\mu M$.

lon Mobility Mass Spectrometry and Data Processing. Mass spectra were acquired on a Thermo Scientific HF Orbitrap mass spectrometer modified to perform UVPD in the HCD cell, similar to that described previously. Borosilicate tips were pulled in-house and coated in gold/palladium for nanoelectrospray ionization. The voltage applied for ESI was supplied by an external power supply using 0.8–1.5 kV greater than the highest potential applied to the drift tube. All UVPD was performed using a single 1.5 mJ laser pulse from a 193 nm ArF Excimer laser (Coherent ExciStar XS 500). Examples of MS1 and UVPD mass spectra are shown in Figures S1–S9.

The low-pressure drift tube is described in detail elsewhere⁵⁰ and is shown in Figure S10. In brief, the instrument is comprised of two RF ion funnels mounted on either end of an approximately 1-m-long drift region consisting of three modular sections. While traditional FT-IMS experiments use a linear frequency sweep for modulating the two ion gates of the DT-IMS system, synchronized stepped frequency modulation was implemented to allow averaging of UVPD spectra. 51 Raw IM-UVPD-MS data files were deconvoluted and searched against the corresponding protein sequence using Prosight PC (see the workflow scheme in Figure S11). The resulting matching fragment list, which includes both the intact monoisotopic mass and m/z of each fragment (Table S1), was imported into a custom data processing program written in Matlab along with the corresponding mzXML files containing the raw MS data. Any ATD with a signal-to-noise ratio below 3 was removed. For UVPD experiments, the precursor ion ATD was fit to three Gaussians to represent three conformational states, and the area of each was calculated to represent the abundance of that conformational state. The areas were plotted as bars based on the backbone position that was cleaved to generate the fragment ions, and the heights of the bars reflect the relative contributions of the conformational state of the precursor ion to each fragment ion. More details are provided in the Supporting Information.

■ RESULTS AND DISCUSSION

Mobility-resolved UVPD was undertaken for two proteins, ubiquitin and myoglobin. Ubiquitin has been extensively characterized both in solution and the gas phase by numerous

methods, including IM with and without UVPD. 43,46,52,53 The 8+ charge state of ubiquitin was selected as a benchmark protein as it has been the focus of a number of past studies and is known to adopt several distinct gas-phase structures. 53,54 A sweep utilizing the stepped frequency generator from 5 to 1000 Hz, allowing 3 ms averages at each frequency step, was performed while acquiring UVPD mass spectra using a single 1.5 mJ pulse with a fixed ion accumulation time of 500 ms and a resolution of 120 000 for the mass spectra. Data were processed as described in the Methods section of the Supporting Information to produce ATDs for 123 fragment ions (Figure S12). Of these, 45 did not meet the signal-to-noise criteria of 3 and were eliminated, leaving ATDs of 78 fragment ions for further analysis. These 78 fragment ions included 30 a-ions, 1 b-ion, 27 x-ions, 6 y-ions, and 12 z-ions, in total, representing backbone cleavages between 66 of 77 pairs of residues (85% sequence coverage).

The ATD of the 8+ charge state of ubiquitin was fit using three Gaussian peaks, as shown in detail elsewhere to represent known conformations, 53,54 centered at $t_d = 31.8$, 35.0, and 36.5 ms, as illustrated in Figure 1A. The first of these (purple, Peak 1) is believed to represent the more folded native conformation (Nstate), while the second peak likely represents the largely helical A-state known to be dominant in acidic water-methanol solutions (Peak 2, green). 53,54 The third state (blue peak) is believed to represent the lesser-studied B-state, believed to be an unfolded variety of the A-state or some other more elongated conformation. Based on molecular dynamics (MD) simulations published previously, 43 two distinct subconformations of the Astate that arise from Pro¹⁹ adopting a *cis* or *trans* stereochemistry produce sufficient changes in the structure to be partially resolved by IM. The ATD of the precursor ion was also fit using two or four Gaussian peaks, in each case yielding less satisfactory

The ATDs of the 78 fragment ions were fit to the same three Gaussians of the precursor ATD, while the peak widths were allowed to vary to represent the relative amounts of each conformation. Examples of ATDs of two fragment ions (x_{41}^{5+}) originating from backbone cleavage G35/I36 and a66 originating from backbone cleavage T66/L67) with fit Gaussians are shown in Figure 1B. Based on triplicate measurements, relative standard deviations of the areas of the three fit peaks ranged from 1 to 27%, averaging 12% for the 78 fragment ions. To facilitate visualization of the pattern of peak profiles for all of the observed fragment ions, the areas of the three Gaussian fit peaks for each fragment ion were compared to the corresponding peak areas of the three Gaussians of the precursor ion (ubiquitin, 8+), as described in the Experimental Section. These normalized comparison values were plotted as a histogram for N-terminal and C-terminal fragment ions as a function of protein backbone position in Figure 1D. Bars close to a value of 1 (dashed black lines in Figure 1D) indicate peak areas of fragment ions that are similar to those of the precursor profile. Bars that deviate from 1 suggest regions of structural changes of the protein in which a specific fragmentation pathway (i.e., a backbone cleavage site) is favored or disfavored for a particular precursor conformation.

The peak profile corresponding to the x_{41}^{5+} ion (Figure 1B) closely matches the peak profile of the precursor ion, and the corresponding bars in the lower half of Figure 1D (labeled as x_{41} , G35/I36) are close to unity. The peak profile corresponding to the a_{66}^{6+} ion, corresponding to backbone cleavage at T66/L67, does not exactly mirror the precursor profile, and this is

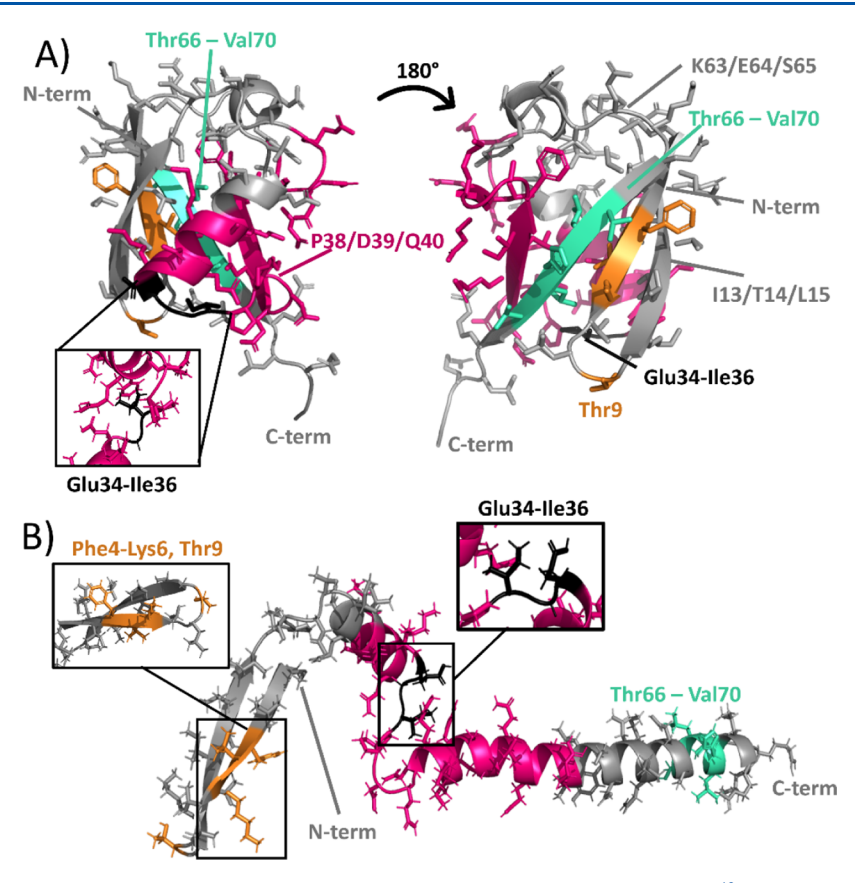


Figure 2. Two conformations of ubiquitin (PDB: 1UBQ): A) N-state and B) the highly helical A-state⁴³ with colors corresponding to sequence sections from Figure 1C. Glu34 and Ile36 (both shaded in black) are magnified for both structures in the insets to display the side-chain interactions with nearby residues.

summarized by the triplet set of bars in Figure 1D (labeled as a_{66} , T66/L67). The abundance of Peak 3 is somewhat enhanced (Figure 1D, greater than dashed y = 1 line), and the abundance of Peak 2 is suppressed (Figure 1D, less than dashed y = 1 line). This change in the overall peak profile for the a_{66}^{6+} ion suggests that the T66/L67 cleavage site is enhanced for the Peak 3 conformation and suppressed for the Peak 2 conformation. The UVPD mass spectrum of ubiquitin (8+) and the entire compilation of fragment ions, their m/z values, abundances, and charge states, as well as their ATDs, peak areas, and standard deviations, are included in Figures S4 and S12 as well as in Table S1. Every backbone cleavage site (corresponding to specific fragment ions) that appears in Figure S4 may not be observed in Figure 1D owing to the signal-to-noise cutoff used for the processed ATDs for the ion mobility data.

As shown previously, the 8+ charge state of ubiquitin, even under denaturing conditions, can display a variety of conformations from native-like folded conformations to fully denatured states. The variation in mobilities for these different conformations is reflected in the three Gaussian peaks in Figure 1, representing the N-state (Peak 1), A-state (Peak 2), and presumed B-state (or other elongated conformation) (Peak 3) of ubiquitin (8+) reported in prior studies. The A-state is often heavily favored for the 8+ charge state of ubiquitin sprayed from water/methanol solutions, represented in Figure 1A as Peak 2. The abundance of the folded, more compact native N-state (Peak 1) is significantly lower than the abundances of the other conformational states (Peaks 2 and 3) owing to the denaturing 50% methanol solution. The more unfolded B-state is represented as Peak 3, corresponding to the longest drift time

within the ATD and therefore representing the most elongated structure(s). This B-state has been noted to be generated in solutions containing methanol and retains structural elements of both an entirely unfolded, structureless U-state and the helical A-state.⁵³

Direct comparison of the normalized peak areas for given conformations can point to regions of the protein for which fragmentation may vary based on the protein's secondary structure and/or conformational motif. While minimal variations (not statistically significant) in the normalized peak area are observed for fragment ions spanning much of the protein backbone, 35 fragment ions display areas (i.e., abundances) that differ by more than 20% for the Peak 1 area compared to its expected area based on the area of the precursor Peak 1; 41 fragment ions exhibit differences greater than 20% in the area of Peak 2 compared to the expected area based on the area of the precursor Peak 2; 48 fragments exhibit differences greater than 20% of the area of Peak 3 when compared to its expected area based on the area of precursor Peak 3. These fragment ions that display higher or lower than expected abundances correspond to ones for which fragmentation is enhanced or suppressed for a particular precursor conformation. These particular fragment ions (35 for Peak 1, 41 for Peak 2, and 48 for Peak 3) are summarized in Table S1. Additionally, the greatest variations occur for Peaks 2 and 3 corresponding to specific segments of the protein backbone, while Peak 1 areas, in comparison, display less apparent variation, likely due to the generally low abundance of the folded N-state conformers for the 8+ charge state of ubiquitin.

The first region of significance spans Phe4 to Gly10 (Figure 1C, with residues coded in orange font in the sequence and the stretch underlined in orange font in Figure 1D). Fragment ions and ATDs that originated from backbone cleavages in this Nterminal region (with sufficient signal-to-noise) are included in Table S1. This region encompasses the first of the two Nterminal β -strands along with the first loop region. Fragmentation is notably enhanced for the more elongated B-state (Peak 3) when compared to the A-state (Peak 2), as exemplified by fragment ions $(a_4 + 1)^+$ (F4/V5 cleavage) and $(a_6 + 1)^+$ (K6/T7 cleavage) in Figure 1D. The locations of the backbone cleavages that produce these fragment ions are also shaded in orange on the putative structures of native (Figure 2A) and A-state (Figure 2B) conformations. Examination of the N-state protein structure reveals that these residues are within 5 Å in space of multiple other regions of the protein, likely participating in numerous noncovalent intramolecular interactions, which induce greater stability and suppress fragmentation for this conformation. In contrast, this region of the A-state structure is more elongated, and residues Phe4, Val5, and Lys6 only interact with the second β -strand (residues Gly10 to Val17), resulting in fewer noncovalent interactions and facilitating the cleavage and release of the fragment ions in greater abundance than the Nstate conformation. The abundance of fragment ions observed for the B-state conformation is even greater than those of the Astate, suggesting minimal to no interaction of this region of the protein with surrounding residues. While the structure of this Bstate is not known in detail, increases in fragmentation in these regions suggest significant structural differences from the other states and imply that this region may be more unstructured, akin to the known U-state of ubiquitin. In the regions where the fragmentation of the B-state (Peak 3) is similar to that of the Astate (Peak 2) and mirrors the corresponding peak area distribution of the precursor, we postulate that these structural regions are similar for the A-state and B-state.

Backbone cleavages between Glu34 and Gly35 and Gly35 and Ile36, three residues that comprise another loop region bridging two α -helical structures (and denoted by the black segment of the protein sequence), produce z_{42}^{5+} and x_{41}^{5+} fragment ions. The peak profiles (i.e., abundances of Peaks 1, 2, and 3) for these two prominent fragment ions mirror the peak profile observed for the precursor ion (Figure 1D, normalized fractional areas are all close to y=1). While this loop region is critical to the A-state structure overall, it is likely mirrored within the B-state structure as well. This suggests that this region does not contribute to significant structural differences among the three conformations of the protein.

From the middle third of the protein sequence (residue 26) to the C-terminus, enhanced fragmentation is observed for the elongated B-state conformation (Peak 3) across a majority of backbone sites, locations denoted by the pink and teal segments in Figure 1C. This large region also has the same shaded colors in Figure 2 on the protein crystal structures for comparison. Between Val26 and the C-terminus, 38 backbone sites were cleaved by UVPD, with 29 exhibiting enhanced fragmentation for Peak 3, including backbone sites Val26/Lys27, Lys27/Ala28, Ile30/Gln31, Gln31/Asp32, Lys33/Glu34, Glu34/Gly35, Ile36/Pro37, Pro37/Pro38, Pro38/Asp39, Asp39/Gln40, Gln40/Gln41, Leu43/Ile44, Ile44/Phe45, Phe45/Ala46, Ala46/Gly47, Gly47/Lys48, Gln49/Leu50, Leu50/Glu51, Glu51/Asp52, Arg54/Thr55, Asp58/Tyr59, Tyr59/Asn60, Asn60/Ile61, Ile61/Gln62, Gln62/Lys63, Ser65/Thr66, Thr66/Leu67, Leu67/His68, and Arg72/Leu73. The increase

in B-state fragmentation in comparison to the two other conformers suggests that the protein adopts a different, more open structure in this region, allowing ready production and release of fragment ions owing to fewer noncovalent interactions. This region of the A-state consists of a long α -helical secondary structure that, although highly structured, contains fewer intermolecular interactions with neighboring regions of the protein than the compact N-state, allowing increased fragmentation.

Across the majority of the protein backbone, fragmentation of the N-state is suppressed relative to the A- and B-states, supporting a compact, folded conformation with significant noncovalent interactions that stabilize the protein and impede the release of fragment ions even if a backbone site is cleaved. While the B-state structure is not well characterized, the IM-UVPD strategy has shown that regions of minimal structural organization are likely present in the N-terminus region of the protein (e.g., Phe4 to Lys6) and throughout a majority of the region from Ile36 to the C-terminus.

A second protein, apo-myoglobin (16.9 kDa), was analyzed using the same strategy and parameters employed for the analysis of ubiquitin. The 15+ charge state was targeted as it has been previously shown to exhibit a complex arrival time distribution, suggesting at least two dominant conformations of the protein. 12 The ATDs were again fit to three Gaussians to accommodate an array of features that contribute to a somewhat broad profile, as has been observed previously for the 15+ charge state of apo-myoglobin, 12,55,56 of which the two abundant conformations were further analyzed. Figure S13 shows the fitted ATDs for all of the fragments generated. Figure S14 shows the ATD for the precursor 15+ charge state of myoglobin along with ATD profiles of eight z-type fragment ions. Significant variations in the ATD profiles are observed for this subset of zions. The variations in each ATD profile of a particular z-ion and differences among the profiles for the whole series of z-ions suggest a complex interplay between the set of structures adopted by myoglobin in the gas phase and subtle conformational changes that influence the protein fragmentation, presumably mediated by adjustments in the noncovalent interactions associated with each subpopulation. For example, the abundance of the z_{28} fragment ion (originating from Ala125/ Asp126 backbone cleavage) is greater for the intermediate compact conformation, whereas the abundance of the z_{33} ion (produced from Pro120/Gly121 cleavage) is greater for the most extended conformation. This series of residues between the C-terminus and Ala125 corresponds to an α -helix region of myoglobin in its native form, but the backbone cleavage site for the z_{33} ion is closer to the adjacent loop, which may have fewer stabilizing interactions for the more unfolded structure, enhancing fragmentation at that site. The abundance of z₁₃ (corresponding to cleavage between Asn140/Asp141) is greatest for the most compact conformation (i.e., shortest drift time) and does not significantly overlap with the conformational distributions of any of the other fragment ions. Enhanced fragmentation of the C- and N-terminus regions is often a signature of protein fraying in the gas phase, often the only significant region of fragmentation for the most compact structures. The ATD profiles of the other z-ions also show rather remarkable variations, ones likely reflecting reorganization of the local network of noncovalent interactions associated with each feature of the protein, as evidenced by how readily the nascent fragment ions are released and detected upon backbone cleavages induced by UVPD.

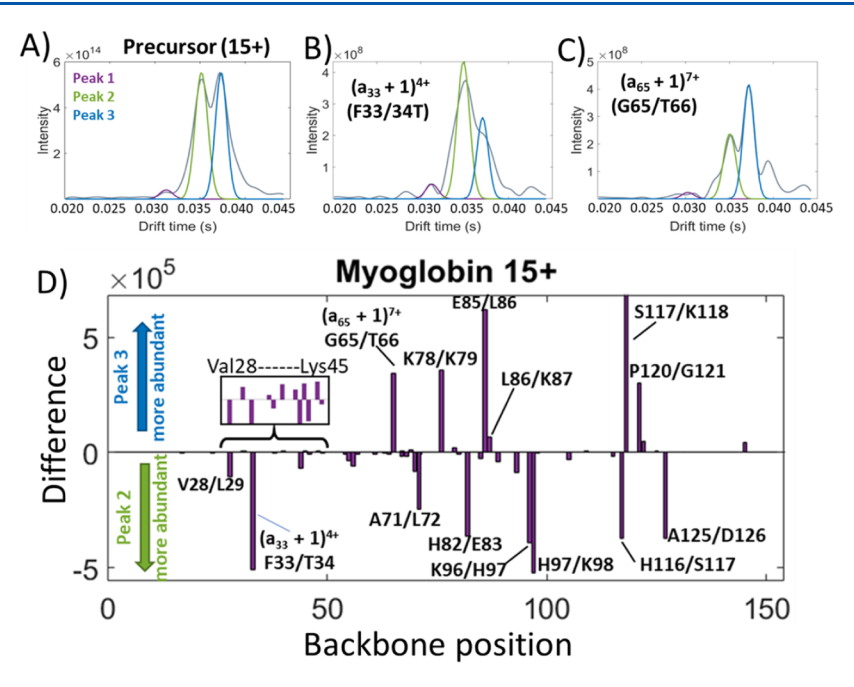


Figure 3. A) Precursor ATD for the 15+ charge state of myoglobin fits to three Gaussian peaks (purple, green, blue). The unprocessed ATD is shown in gray. B,C) ATDs, generated from two fragments of the 15+ charge state of myoglobin, fit to the same three Gaussian peaks, allowing the widths to vary based on the fit. D) Difference plot showing changes in signal intensities of the ATDs for specific fragment ions comparing Peaks 2 and 3. Bars greater than 0 indicate greater intensities for Peak 3, whereas bars less than 0 indicate greater intensities for Peak 2.

Considering the entire compilation of ion mobility/UVPD data for myoglobin, ATDs were generated for a total of 157 fragment ions. Among these, 28 did not meet the standard signal-to-noise criteria of 3 and were discarded, leaving ATDs of 129 fragment ions corresponding to 69 a-ions, 1 b-ion, 19 x-ions, 14 y-ions, and 26 z-ions, totaling 60% sequence coverage. The ATDs were fitted to a set of three Gaussian profiles to allow more detailed differentiation of the subpopulations of conformations. Figure 3A shows the unprocessed ATD for the 15+ charge state of myoglobin in gray along with the three fit Gaussian profiles in purple (shortest drift time; most compact conformer and lowest abundance), green (intermediate drift time; intermediate conformer), and blue (longest drift time; most elongated conformer). Based on the areas of Peaks 2 and 3, these intermediate and elongated conformers have similar abundances. For the fragment ions generated by UVPD, significant differences in relative abundances are observed based on the ATDs for Peak 2 (green) and Peak 3 (blue), whereas Peak 1 consistently exhibited fragment ions of low abundance. The Gaussian fits of the ATDs for two representative fragments, $(a_{33} + 1)^{4+}$ originating from backbone cleavage Phe33/Thr34 and $(a_{65} + 1)^{7+}$ originating from backbone cleavage Gly65/Thr66, are shown in Figure 3B. For the a₃₃ ion, the abundance is significantly greater for the Peak 2 conformer than the Peak 3 conformer, and for the a₆₅ ion, the abundance is substantially greater for the Peak 3 conformer than the Peak 2 conformer. The difference between the areas of ATD peaks 2 and 3 was calculated for each fragment ion and is mapped along the protein backbone in Figure 3D as a difference plot, with positive values indicating greater fragment ion abundances for the more unfolded Peak 3 conformation and negative values corresponding to greater fragment ion abundance of the more compact Peak 2 conformation.

The regions of the protein that exhibited the greatest differences in fragmentation tended to be loop regions connecting longer α -helical strands, whereas the more

structured helix regions are stabilized by extensive intramolecular interactions that suppress fragmentation (or impede the release of fragment ions even if a backbone site is cleaved). The differences in backbone fragmentation spanning residues Val28—Lys45 are expanded in the inset of Figure 3D. A majority of this stretch of the protein exhibits no significant differences (near zero) in fragmentation for the Peak 2 and Peak 3 conformations, but there are two substantial differences corresponding to cleavages at Val28/Leu29 (a282+ ion) and Phe33/Thr34 (a₃₃⁴⁺ ion). This segment of myoglobin contains a proline residue, Pro37, that may create a kink, resulting in an \sim 50° bend in the sequence. The strain of this region is likely counteracted by intramolecular interactions between side chains before and after the kink. These attributes likely contribute to a compact local structure for the conformations associated with Peaks 2 and 3. The backbone cleavage sites Val28/Leu29 and Phe33/Thr34, which resulted in significantly more fragmentation for Peak 2 compared to Peak 3, suggest a degree of local reorganization that facilitated backbone cleavage and release of fragment ions for the Peak 2 conformer.

Similarly, the region spanning residues Leu89–Glu105 (Figure 3D) displays enhanced fragmentation for the Peak 2 conformation, suggesting a less compact local structure. In contrast, fragments resulting from cleavage of residues Gly65/Thr66, Leu86/Lys87, Ser117/Lys118, and Pro120/Gly121 all show greater areas for Peak 3 than Peak 2, corresponding to enhanced fragmentation in these short spans and indicating a more elongated or less structured conformation. Interestingly, each of these residues is adjacent to or near neighbors of proline and glycine residues, all known to play significant roles in α -helical formation. The increased area of Peak 3 for fragments that originate from backbone cleavage at Pro120 (z_{33}^{4+} and x_{33}^{4+}) further suggests the possibility of cis/trans isomerization, especially in the residues contained in the center of the α -helical strands. Induced trans conformations may contribute to the

elongated protein structure as well as the high abundance of UVPD fragments.

Cleavage of specific backbone sites also varies with the precursor charge state, an outcome that further reflects variations in the conformational distribution as a function of the precursor charge state. Figure S15 shows arrival time distributions generated for the y_{34} (H119/P120 cleavage site) and $a_{33} + 1$ (F33/T34 cleavage site) fragment ions from five different charge states of apo-myoglobin. As the precursor charge state increases, the drift times of the protein and fragment ions are expected to increase as the protein elongates, owing to greater electrostatic interactions. However, each fragment ion profile displays variations depending on the location of the backbone site that is cleaved, suggesting local structural changes within each protein charge state. The profiles for the two representative fragment ions mirror each other when spawned from the 17+ to 19+ precursor charge states, and there is little evidence for multiple distinctive conformations (Figure S15A,B). In contrast, significantly more variations in the ATD profiles are observed for the fragment ions generated from the 15+ and 16+ charge states, and the profiles of the two targeted fragment ions (y₃₄ and a₃₃) are distinctive from each other. The trend of increasing drift time with decreasing charge state for the two fragment ions seems counterintuitive because ions are expected to elongate with an increasing charge state, thus increasing their drift times. It is possible that the protein undergoes partial collapse, and the resulting fragment ions reflect a portion of the collapsed structure. These observations reiterate that tracking the fragment ion profiles reveals important differences in specific local regions of the protein as a function of charge state (such as the His119/Pro120 backbone cleavage that is mapped by the y_{34} fragment ion and the Phe33/Thr34 backbone cleavage that is mapped by the a_{33} fragment ion).

CONCLUSIONS

A low-pressure drift tube Orbitrap mass spectrometer equipped with 193 nm UVPD was constructed for the analysis of protein conformers based on variations in abundances of fragment ions that track with the conformationally separated precursor ions. Enhancement or suppression of backbone fragmentation is reflected in the abundances of the resulting fragment ions, correlating with the regions of the protein that are more compact or elongated. Through analysis of the 8+ charge state of ubiquitin, three distinct structures consisting of the N-state, Astate, and the less studied B-state were identified. Suppression of fragmentation of the N-state supported a more folded and compact structure, while enhanced fragmentation of the A- and B-states corresponded to more flexible regions with less extensive networks of noncovalent interactions. Additional insights into the structure of the B-state revealed secondary structural motifs that may be retained from the A-state, as well as other sections that are less structured. Analysis of a larger protein, apo-myoglobin, also revealed regions consistent with more elongated structures that exhibited enhanced backbone fragmentation. Some of the ATDs of specific fragment ions displayed remarkable shifts and distinctive features, suggesting very specific, localized changes in conformation that manifested as notable variations in fragmentation by UVPD. Tracking variations in the ATD profiles of selected fragment ions as a function of the protein charge state also uncovered notable differences, again suggesting variations in the conformations. The ability to monitor conformationally specific fragmentation of proteins with high mass accuracy and resolution offers many

opportunities for gaining new insights into structures of proteins in the gas phase.

ASSOCIATED CONTENT

Supporting Information

The Supporting Information is available free of charge at https://pubs.acs.org/doi/10.1021/acs.analchem.4c03119.

Low pressure drift tube instrument description; methods and procedures for data processing; MS1 and UVPD spectra of ubiquitin and myoglobin (Figures S1–S9); instrument schematic containing LPDT and MS (Figure S10); overview of general workflow for IM-UVPD data processing (Figure S11); all fragment ATDs with Gaussian fits (Figures S12 and S13); ATDs from a series of z-type fragment ions (Figures S14 and S15); identification of all UVPD fragment ions through Prosight PC (Table S1) (PDF)

Sequence coverage maps and arrival time distributions of all fragment ions (XLSX)

AUTHOR INFORMATION

Corresponding Author

Jennifer S. Brodbelt — Department of Chemistry, The University of Texas at Austin, Austin, Texas 78712, United States; orcid.org/0000-0003-3207-0217; Email: jbrodbelt@cm.utexas.edu

Authors

Jamie P. Butalewicz — Department of Chemistry, The University of Texas at Austin, Austin, Texas 78712, United States

James D. Sanders – Department of Chemistry, The University of Texas at Austin, Austin, Texas 78712, United States

Kyle J. Juetten – Department of Chemistry, The University of Texas at Austin, Austin, Texas 78712, United States

Nathan W. Buzitis — Department of Chemistry, Washington State University, Pullman, Washington 99164, United States; orcid.org/0009-0009-3510-2887

Brian H. Clowers — Department of Chemistry, Washington State University, Pullman, Washington 99164, United States; occid.org/0000-0002-5809-9379

Complete contact information is available at: https://pubs.acs.org/10.1021/acs.analchem.4c03119

Author Contributions

[#]J.P.B. and J.D.S. contributed equally as first authors.

Notes

The authors declare no competing financial interest.

ACKNOWLEDGMENTS

We acknowledge the following funding sources: NSF (Grant CHE-2203602, JSB), the Welch Foundation (Grant F-1155, JSB), and NIH (R01GM138863, BHC).

REFERENCES

- (1) Lapthorn, C.; Pullen, F.; Chowdhry, B. Z. Mass Spectrom. Rev. **2013**, 32 (1), 43–71.
- (2) Wu, Q.; Wang, J.-Y.; Han, D.-Q.; Yao, Z.-P. TrAC, Trends Anal. Chem. 2020, 124, 115801.
- (3) Young, L. M.; Saunders, J. C.; Mahood, R. A.; Revill, C. H.; Foster, R. J.; Tu, L.-H.; Raleigh, D. P.; Radford, S. E.; Ashcroft, A. E. *Nat. Chem.* **2015**, *7* (1), 73–81.

- (4) Kyle, J. E.; Zhang, X.; Weitz, K. K.; Monroe, M. E.; Ibrahim, Y. M.; Moore, R. J.; Cha, J.; Sun, X.; Lovelace, E. S.; Wagoner, J.; Polyak, S. J.; Metz, T. O.; Dey, S. K.; Smith, R. D.; Burnum-Johnson, K. E.; Baker, E. S. *Analyst* **2016**, *141* (5), 1649–1659.
- (5) Leaptrot, K. L.; May, J. C.; Dodds, J. N.; McLean, J. A. Nat. Commun. 2019, 10 (1), 1-9.
- (6) Paglia, G.; Angel, P.; Williams, J. P.; Richardson, K.; Olivos, H. J.; Thompson, J. W.; Menikarachchi, L.; Lai, S.; Walsh, C.; Moseley, A.; Plumb, R. S.; Grant, D. F.; Palsson, B. O.; Langridge, J.; Geromanos, S.; Astarita, G. *Anal. Chem.* **2015**, 87 (2), 1137–1144.
- (7) Wyttenbach, T.; von Helden, G.; Bowers, M. T. J. Am. Chem. Soc. 1996, 118 (35), 8355-8364.
- (8) Wu, C.; Siems, W. F.; Klasmeier, J.; Hill, H. H. Anal. Chem. 2000, 72 (2), 391–395.
- (9) Baker, E. S.; Livesay, E. A.; Orton, D. J.; Moore, R. J.; Danielson, W. F.; Prior, D. C.; Ibrahim, Y. M.; LaMarche, B. L.; Mayampurath, A. M.; Schepmoes, A. A.; Hopkins, D. F.; Tang, K.; Smith, R. D.; Belov, M. E. J. Proteome Res. 2010, 9 (2), 997–1006.
- (10) Angel, T. E.; Aryal, U. K.; Hengel, S. M.; Baker, E. S.; Kelly, R. T.; Robinson, E. W.; Smith, R. D. *Chem. Soc. Rev.* **2012**, 41 (10), 3912.
- (11) Covey, T.; Douglas, D. J. J. Am. Soc. Mass Spectrom. 1993, 4 (8), 616-623.
- (12) May, J. C.; Jurneczko, E.; Stow, S. M.; Kratochvil, I.; Kalkhof, S.; McLean, J. A. Int. J. Mass Spectrom. 2018, 427, 79.
- (13) Calabrese, A. N.; Speechley, L. A.; Pukala, T. L. Aust. J. Chem. **2012**, 65 (5), 504.
- (14) Schenk, E. R.; Almeida, R.; Miksovska, J.; Ridgeway, M. E.; Park, M. A.; Fernandez-Lima, F. *J. Am. Soc. Mass Spectrom.* **2015**, *26* (4), 555–563.
- (15) Poltash, M. L.; McCabe, J. W.; Shirzadeh, M.; Laganowsky, A.; Clowers, B. H.; Russell, D. H. *Anal. Chem.* **2018**, *90* (17), 10472–10478.
- (16) Borges-Alvarez, M.; Benavente, F.; Vilaseca, M.; Barbosa, J.; Sanz-Nebot, V. J. Mass Spectrom. 2013, 48 (1), 60-67.
- (17) Bush, M. F.; Hall, Z.; Giles, K.; Hoyes, J.; Robinson, C. V.; Ruotolo, B. T. Anal. Chem. **2010**, 82 (22), 9557–9565.
- (18) Ruotolo, B. T.; Benesch, J. L. P.; Sandercock, A. M.; Hyung, S.-J.; Robinson, C. V. *Nat. Protoc.* **2008**, *3* (7), 1139–1152.
- (19) Makarov, A.; Denisov, E.; Lange, O. J. Am. Soc. Mass Spectrom. **2009**, 20 (8), 1391–1396.
- (20) Frese, C. K.; Altelaar, A. F. M.; van den Toorn, H.; Nolting, D.; Griep-Raming, J.; Heck, A. J. R.; Mohammed, S. *Anal. Chem.* **2012**, 84 (22), 9668–9673.
- (21) Ledvina, A. R.; Beauchene, N. A.; McAlister, G. C.; Syka, J. E. P.; Schwartz, J. C.; Griep-Raming, J.; Westphall, M. S.; Coon, J. J. *Anal. Chem.* **2010**, 82 (24), 10068–10074.
- (22) Madsen, J. A.; Boutz, D. R.; Brodbelt, J. S. J. Proteome Res. 2010, 9 (8), 4205-4214.
- (23) Shaw, J. B.; Li, W.; Holden, D. D.; Zhang, Y.; Griep-Raming, J.; Fellers, R. T.; Early, B. P.; Thomas, P. M.; Kelleher, N. L.; Brodbelt, J. S. J. Am. Chem. Soc. **2013**, 135 (34), 12646–12651.
- (24) Cammarata, M. B.; Thyer, R.; Rosenberg, J.; Ellington, A.; Brodbelt, J. S. J. Am. Chem. Soc. **2015**, 137 (28), 9128–9135.
- (25) Brodbelt, J. S.; Morrison, L. J.; Santos, I. Chem. Rev. 2020, 120, 3328.
- (26) Sanders, J. D.; Mullen, C.; Watts, E.; Holden, D. D.; Syka, J. E. P.; Schwartz, J. C.; Brodbelt, J. S. *Anal. Chem.* **2020**, 92 (1), 1041–1049.
- (27) Kanu, A. B.; Dwivedi, P.; Tam, M.; Matz, L.; Hill, H. H. J. Mass Spectrom. **2008**, 43 (1), 1–22.
- (28) Morrison, K. A.; Siems, W. F.; Clowers, B. H. *Anal. Chem.* **2016**, 88 (6), 3121–3129.
- (29) Keelor, J. D.; Zambrzycki, S.; Li, A.; Clowers, B. H.; Fernández, F. M. *Anal. Chem.* **2017**, *89* (21), 11301–11309.
- (30) Butalewicz, J. P.; Sanders, J. D.; Clowers, B. H.; Brodbelt, J. S. J. Am. Soc. Mass Spectrom. **2023**, 34 (1), 101–108.
- (31) Ibrahim, Y. M.; Garimella, S. V. B.; Prost, S. A.; Wojcik, R.; Norheim, R. V.; Baker, E. S.; Rusyn, I.; Smith, R. D. *Anal. Chem.* **2016**, 88 (24), 12152–12160.

- (32) Clowers, B. H.; Siems, W. F.; Hill, H. H.; Massick, S. M. Anal. Chem. **2006**, 78 (1), 44–51.
- (33) Kwantwi-Barima, P.; Reinecke, T.; Clowers, B. H. Int. J. Ion Mobility Spectrom. **2020**, 23 (2), 133–142.
- (34) McCabe, J. W.; Mallis, C. S.; Kocurek, K. I.; Poltash, M. L.; Shirzadeh, M.; Hebert, M. J.; Fan, L.; Walker, T. E.; Zheng, X.; Jiang, T.; Dong, S.; Lin, C.-W.; Laganowsky, A.; Russell, D. H. *Anal. Chem.* **2020**, 92 (16), 11155–11163.
- (35) McCabe, J. W.; Jones, B. J.; Walker, T. E.; Schrader, R. L.; Huntley, A. P.; Lyu, J.; Hoffman, N. M.; Anderson, G. A.; Reilly, P. T. A.; Laganowsky, A.; Wysocki, V. H.; Russell, D. H. J. Am. Soc. Mass Spectrom. 2021, 32 (12), 2812–2820.
- (36) Cannon, J. R.; Cammarata, M. B.; Robotham, S. A.; Cotham, V. C.; Shaw, J. B.; Fellers, R. T.; Early, B. P.; Thomas, P. M.; Kelleher, N. L.; Brodbelt, J. S. *Anal. Chem.* **2014**, *86* (4), 2185–2192.
- (37) Greer, S. M.; Brodbelt, J. S. *J. Proteome Res.* **2018**, *17* (3), 1138–1145.
- (38) Cleland, T. P.; DeHart, C. J.; Fellers, R. T.; VanNispen, A. J.; Greer, J. B.; LeDuc, R. D.; Parker, W. R.; Thomas, P. M.; Kelleher, N. L.; Brodbelt, J. S. *J. Proteome Res.* **2017**, *16* (5), 2072–2079.
- (39) Sipe, N. S.; Brodbelt, S. J. Phys. Chem. Chem. Phys. **2019**, 21 (18), 9265–9276.
- (40) Mehaffey, M. R.; Sanders, J. D.; Holden, D. D.; Nilsson, C. L.; Brodbelt, J. S. Anal. Chem. **2018**, 90 (16), 9904–9911.
- (41) Morrison, L. J.; Brodbelt, J. S. J. Am. Chem. Soc. 2016, 138 (34), 10849–10859.
- (42) Greisch, J. F.; Tamara, S.; Scheltema, R. A.; Maxwell, H. W.; Fagerlund, R. D.; Fineran, P. C.; Tetter, S.; Hilvert, D.; Heck, A. J. *Chem. Sci.* **2019**, *10* (30), 7163–7171.
- (43) Warnke, S.; Baldauf, C.; Bowers, M. T.; Pagel, K.; von Helden, G. J. Am. Chem. Soc. **2014**, 136 (29), 10308–10314.
- (44) Warnke, S.; von Helden, G.; Pagel, K. PROTEOMICS **2015**, 15 (16), 2804–2812.
- (45) Theisen, A.; Yan, B.; Brown, J. M.; Morris, M.; Bellina, B.; Barran, P. E. *Anal. Chem.* **2016**, *88* (20), *9964*–*9971*.
- (46) Theisen, A.; Black, R.; Corinti, D.; Brown, J. M.; Bellina, B.; Barran, P. E. J. Am. Soc. Mass Spectrom. **2019**, 30 (1), 24–33.
- (47) Morrison, K. A.; Bendiak, B. K.; Clowers, B. H. J. Am. Soc. Mass Spectrom. **2017**, 28 (4), 664–677.
- (48) Sanders, J. D.; Shields, S. W.; Escobar, E. E.; Lanzillotti, M. B.; Butalewicz, J. P.; James, V. K.; Blevins, M. S.; Sipe, S. N.; Brodbelt, J. S. *Anal. Chem.* **2022**, *94* (10), 4252–4259.
- (49) Fort, K. L.; Dyachenko, A.; Potel, C. M.; Corradini, E.; Marino, F.; Barendregt, A.; Makarov, A. A.; Scheltema, R. A.; Heck, A. J. R. *Anal. Chem.* **2016**, 88 (4), 2303–2310.
- (50) Buzitis, N. W.; Clowers, B. H. J. Am. Soc. Mass Spectrom. **2024**, 35 (4), 804–813.
- (51) Cabrera, E. R.; Clowers, B. H. J. Am. Soc. Mass Spectrom. 2022, 33 (3), 557-564.
- (52) Sobott, F.; Watt, S. J.; Smith, J.; Edelmann, M. J.; Kramer, H. B.; Kessler, B. M. J. Am. Soc. Mass Spectrom. **2009**, 20 (9), 1652–1659.
- (53) Shi, H.; Clemmer, D. E. J. Phys. Chem. B **2014**, 118 (13), 3498–3506.
- (54) Shi, H.; Pierson, N. A.; Valentine, S. J.; Clemmer, D. E. J. Phys. Chem. B **2012**, 116 (10), 3344–3352.
- (55) Vahidi, S.; Stocks, B. B.; Konermann, L. Anal. Chem. **2013**, 85 (21), 10471–10478.
- (56) Schenk, E. R.; Almeida, R.; Miksovska, J.; Ridgeway, M. E.; Park, M. A.; Fernandez-Lima, F. J. Am. Soc. Mass Spectrom. 2015, 26, 555–563